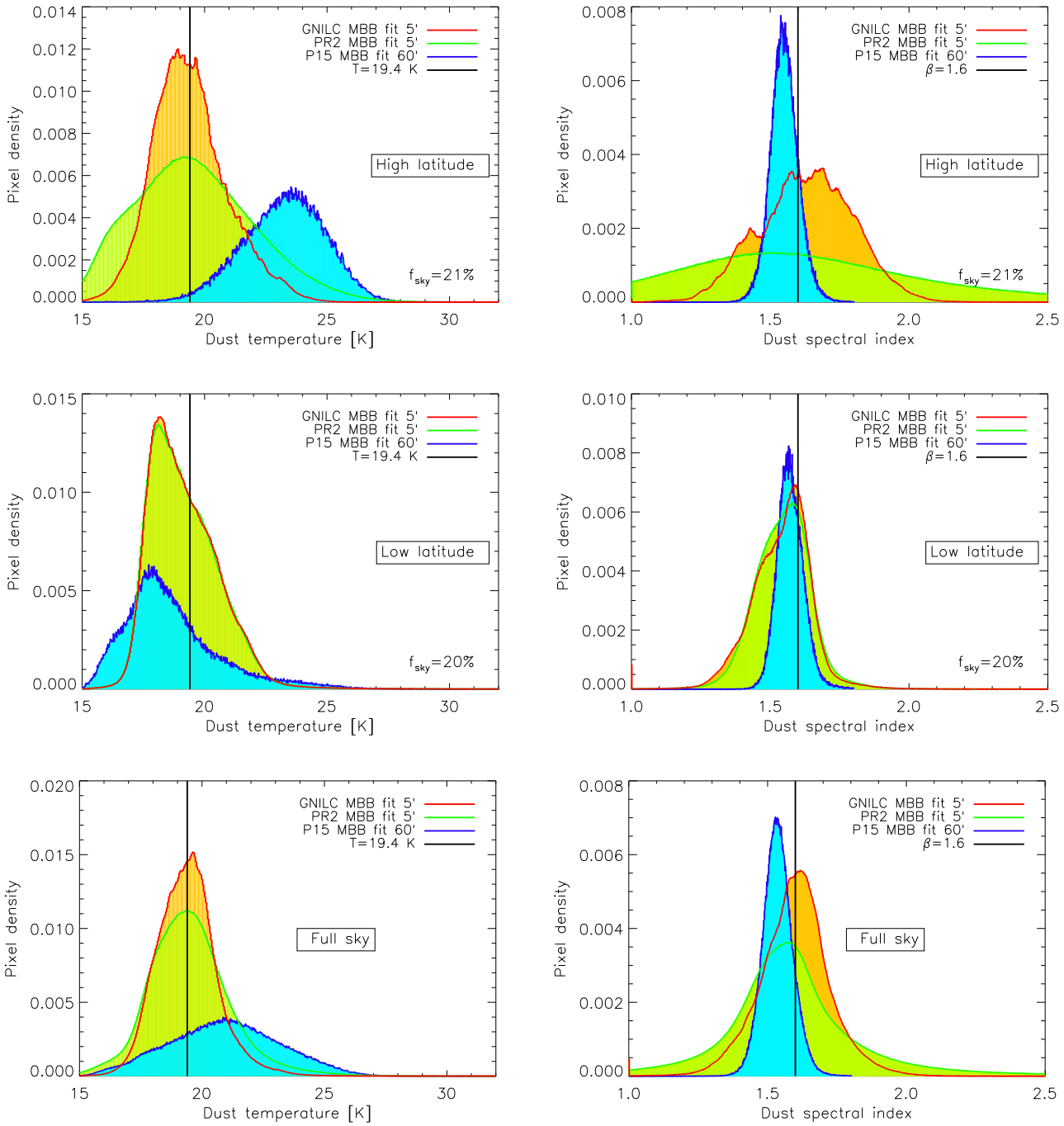

Fig. 11. Normalized histograms of $T_{\rm dust}$ and $\beta_{\rm dust}$ at 5′ resolution for the GNILC MBB fit (red contours) and the PR2 MBB fit a la model P13 (green contours). The normalized histograms for the dust model P15 (Commander fit at 60′ resolution) are overplotted (blue contours). The histograms are computed from the subset of pixels corresponding to either the high-latitude area in the sky with $f_{\rm sky}$ = 21% (*upper panels*), the low-latitude area in the sky with $f_{\rm sky}$ = 20% (*middle panels*), or the whole sky (*lower panels*). Due to CIB contamination at high-latitude, the PR2 MBB fits show larger dispersion than the GNILC MBB fits in the distributions of $T_{\rm dust}$ and $\beta_{\rm dust}$.

the error bars show the dispersion over the sky of the parameter values.

5. GNILC results on the CIB

5.1. CIB maps

The GNILC method is flexible by allowing either the recovery of the dust map with the CIB-plus-CMB-plus-noise filtered out (shown in this paper) or the recovery of the dust-plus-CIB map with the removal of the CMB-plus-noise only, depending on whether or not one uses the prior on the CIB power spectrum. Therefore, from the difference between the unfiltered GNILC dust-plus-CIB map and the CIB-filtered GNILC dust map we are able to reveal the CIB anisotropies at different frequencies over a large area of the sky. The resulting GNILC CIB maps at 353, 545, and 857 GHz, reconstructed over a large fraction of the sky,

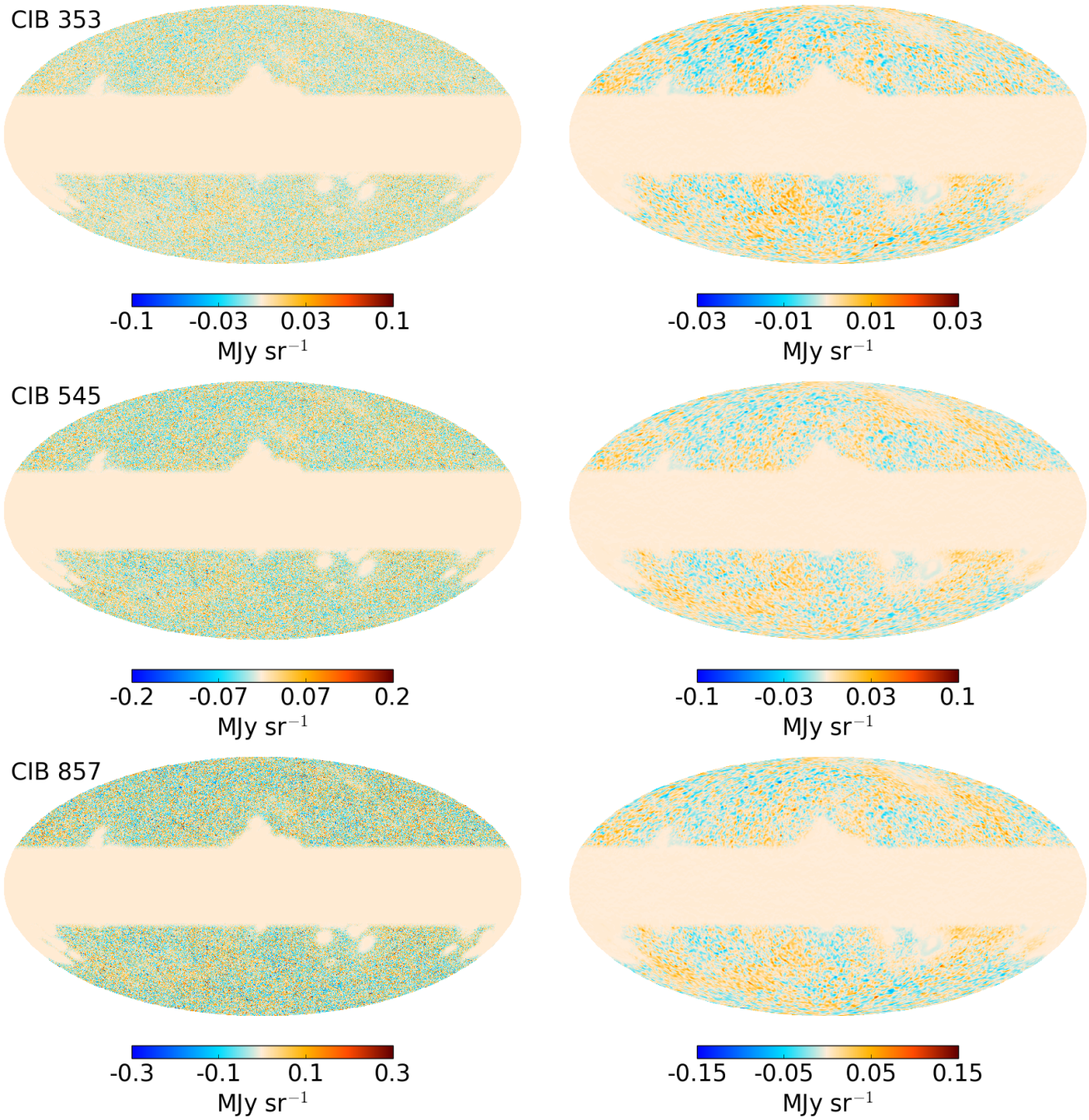

Fig. 12. GNILC CIB maps for a large fraction of the sky at 353 GHz (*top*), 545 GHz (*middle*), and 857 GHz (*bottom*). Apart from thermal dust reconstruction, the GNILC component-separation method gives access to CIB anisotropies over 57% of the sky. The *left panels* show the GNILC CIB maps at full resolution while the *right panels* show the CIB maps smoothed to one degree resolution.

are shown in Fig. 12, both at full resolution and smoothed to 1° resolution. We can see residual zodiacal light emission along the ecliptic plane in the low-resolution CIB maps. This residual comes from the combination by GNILC of different data sets, namely the *Planck*, IRAS, and SFD maps, in which the zodiacal light has been corrected differently. The zodiacal light emission has been reduced in *Planck* data to a negligible level compared to the CMB and dust emissions but is still at a level comparable to the amplitude of the CIB emission.

The GNILC products give us access to the CIB anisotropies on a much larger fraction of the sky (approximately 57%) than the *Planck* CIB maps produced in Planck Collaboration XXX (2014). The GNILC CIB maps can be used as tracers of the dark matter distribution because they allow for an exploration over large areas of the sky of the cross-correlations between CIB and CMB lensing fields (Planck Collaboration XVIII 2014) or between CIB and other tracers of large-scale structure (Serra et al. 2014).

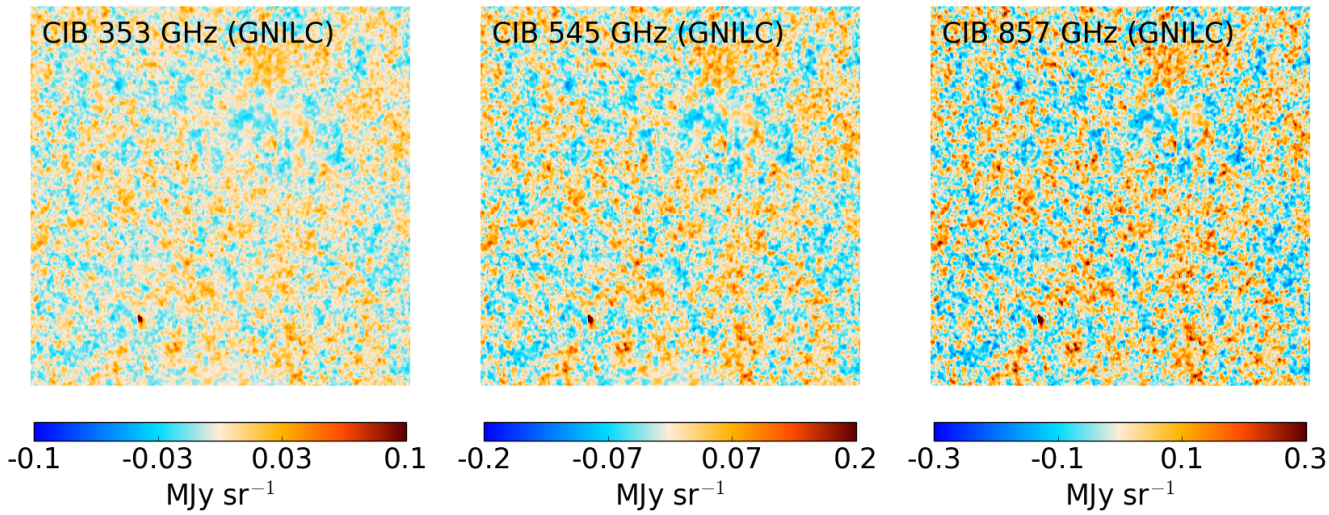

Fig. 13. GNILC CIB maps at 353 GHz (*left*), 545 GHz (*middle*), and 857 GHz (*right*) on a 12.°5 × 12.°5 gnomonic projection of the sky centred at high latitude, $(l, b) = (90°, -80°)$. The partial spatial correlation of the CIB anisotropies between pairs of frequencies is clearly visible. In this figure, the local mean intensity of each map has been subtracted.

In Fig. 13 we show the GNILC CIB maps at 353, 545, and 857 GHz in a high-latitude 12.°5 × 12.°5 region of the sky centred at $(l, b) = (90°, -80°)$. The partial spatial correlation of the CIB anisotropies between pairs of frequencies decreases when the ratio between the two frequencies is further from unity, as expected from the redshift distribution of the CIB anisotropies (Planck Collaboration XXX 2014).

5.2. GNILC CIB versus CIB 2013 in small fields

We now check the consistency between the new GNILC CIB maps and the CIB 2013 maps from Planck Collaboration XXX (2014). In Fig. 14, we compare the GNILC CIB map at 545 GHz with the CIB 2013 map at 545 GHz in four different fields of the Green Bank Telescope H I Intermediate Galactic Latitude Survey (GHIGLS) defined in Martin et al. (2015): Boötes, MC, N1, and SP. The difference map (CIB 2013 − GNILC CIB) is also shown within the same fields. In Fig. 15 we plot the T–T correlation between the GNILC CIB map and the CIB 2013 map in the common fields. We have used a least-squares bisector linear regression (Isobe et al. 1990) for computing the correlation coefficient between both products.

Figures 14 and 15 show that the GNILC CIB maps are consistent with the CIB 2013 maps within the fields considered. In particular the Pearson correlation coefficient between the GNILC CIB maps and the CIB 2013 maps is larger than 0.8 in all fields, with a T–T slope of 0.998 ± 0.005 in the Boötes field, 0.958 ± 0.006 in the MC field, 0.972 ± 0.006 in the N1 field, and 0.935 ± 0.006 in the SP field. Despite the high correlation between the GNILC CIB maps and the CIB 2013 maps within the GHIGLS fields, the correlation is not perfect because both sets of maps were produced from different data releases, respectively PR2 and PR1, for which there have been changes in the calibration coefficients. In addition, estimates of the optical beam resolution have slightly changed between both data releases, therefore not guaranteeing the exact same resolution of both CIB products.

6. Correlations of the CIB and dust maps with the H I map

In the diffuse interstellar medium the dust emission is tightly correlated with the line emission of neutral hydrogen (H I). In this respect, as a tracer of the Galactic dust emission the H I emission map can be used to detect any residual Galactic dust emission in the GNILC CIB maps.

We compute the T–T correlation between the H I map (local plus intermediate velocity clouds) of the LAB survey (Kalberla et al. 2005; Land & Slosar 2007) and the GNILC CIB maps in order to detect any Galactic residual in the reconstructed CIB maps. Figure 16 shows that the correlation between the GNILC CIB map at 353 GHz and the H I map is consistent with zero (Pearson correlation coefficient of 0.004), therefore showing no significant residual Galactic emission in the GNILC CIB map.

We also compute the T–T correlation between the dust map at 353 GHz and the H I map at high Galactic latitude. The high latitude region is defined as the area of the sky where the local beam FWHM of the GNILC dust map is larger than 15′ (Fig. 2). The maps are degraded to HEALPix $N_{\rm side} = 256$.

Figure 17 shows the scatter plot between the H I map and the dust optical depth map for the dust model P13 (green), the PR2 MBB fit (black), and the CIB-filtered GNILC MBB fit (blue). The PR2 MBB fit shows larger scatter than the dust model P13 because in the former the fit is performed in one step at 5′ resolution for all three dust parameters, while in the latter the fit was performed in two steps, with the spectral index first fitted at lower resolution (30′), which slightly reduces the scatter due to CIB contamination. Owing to the large reduction of the CIB contamination in the GNILC maps, the correlation with the H I shows the most reduced scatter.

The particles producing thermal dust emission also cause extinction of the light from stars and quasars, which is quantified by Galactic reddening, $E(B - V)$. We develop a GNILC reddening $E(B - V)$ map by multiplying the GNILC dust optical depth map, τ_{353}, by the factor 1.49×10^{-4} mag derived in Planck Collaboration XI (2014) from the correlation between

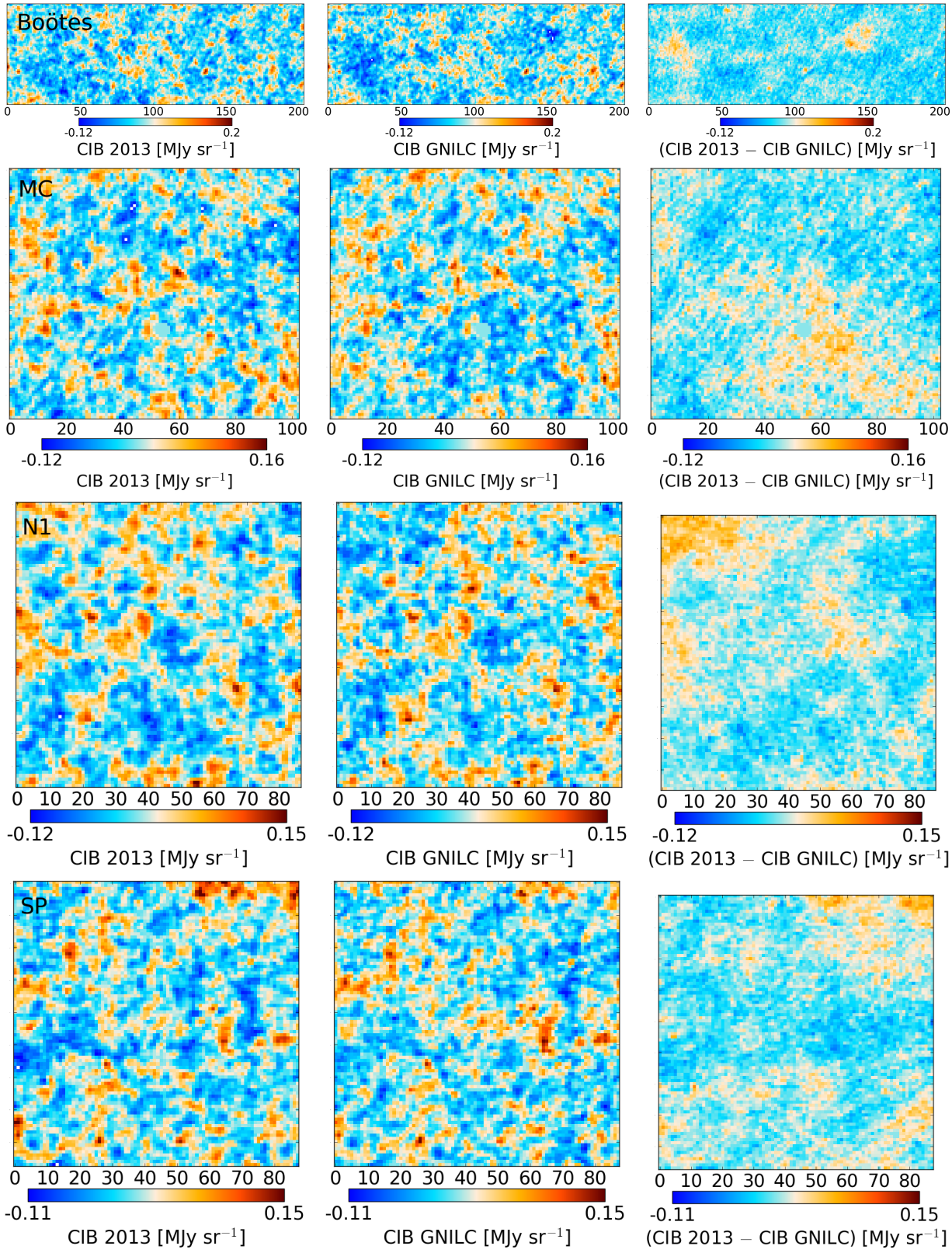

Fig. 14. Maps of cosmic infrared background (CIB) anisotropies in GHIGLS fields (Martin et al. 2015). *Left column*: CIB 2013 (Planck Collaboration XXX 2014). *Middle column*: CIB GNILC. *Right column*: difference (CIB 2013 − GNILC). *From top to bottom row*, the GHIGLS fields are: Boötes; MC; N1; and SP. The size and the location in the sky of each field are defined in Table 1 of Martin et al. (2015).

the reddening of quasars and dust optical depth along the same line of sight. Recently, Green et al. (2015) have produced a three-dimensional dust reddening $E(B-V)$ map based on stars in the Pan-STARRS 1 survey. We projected their three-dimensional

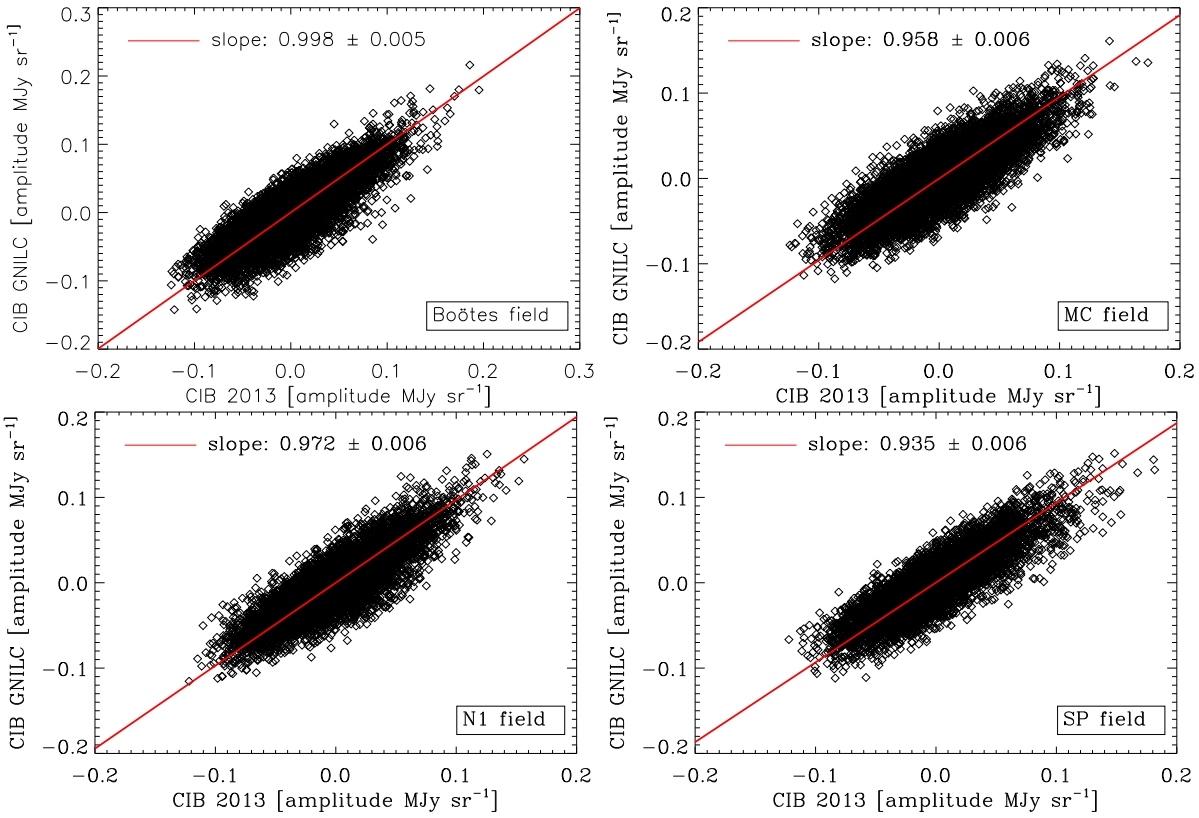

Fig. 15. T–T scatter plot between CIB GNILC and CIB 2013. The fields are Boötes, MC, N1, and SP.

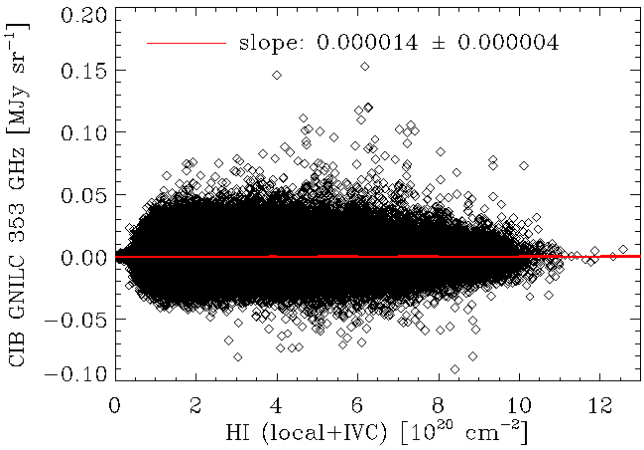

Fig. 16. T–T scatter plot between the H I map and the GNILC CIB map at 353 GHz over 57% of the sky (see Fig. 12).

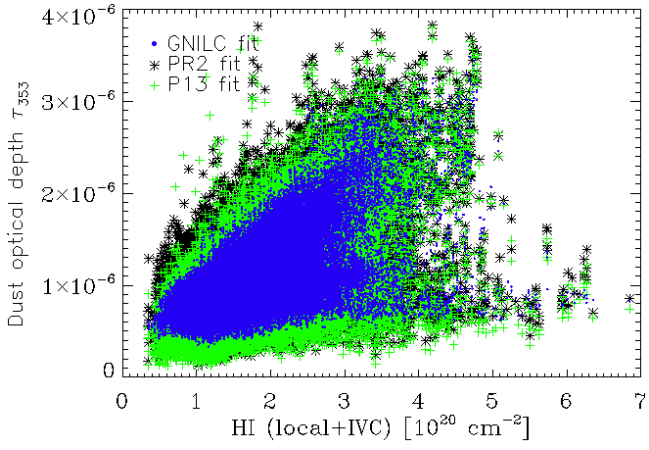

Fig. 17. T–T scatter plot at high Galactic latitude between the H I map and the dust optical depth maps at 353 GHz: dust model P13 (green), PR2 MBB fit (black), GNILC MBB fit (blue). While the slope of the correlation with the H I map is consistent for all the dust optical depth maps, the scatter is smallest for the GNILC dust optical depth map because of the removal of the CIB temperature anisotropies.

dust reddening into a two-dimensional map by computing the median reddening in the farthest distance bin. Figure 18 compares this with the GNILC $E(B-V)$ map, focusing on common area in the north and south Galactic caps where the gas column density is low. Although it shows spatial structure similar to the GNILC $E(B-V)$ map, the $E(B-V)$ map from Green et al. (2015) is noisier. Just as there is a good correlation of τ_{353} and the H I gas column density, $N_{\rm H}$, the correlation of reddening $E(B-V)$ and $N_{\rm H}$ has been long established (e.g., Savage & Jenkins 1972). To explore this further for the low column density area of the sky defined in Fig. 10, in Fig. 19 we plot the ratio $E(B-V)/N_{\rm H}$ binned with respect to $N_{\rm H}$ for both GNILC and the reddening map from Green et al. (2015). For GNILC the trend with $N_{\rm H}$ is quite flat; the horizontal line plotted is compatible with the behaviour for the opacity $\tau_{353}/N_{\rm H}$ found in Planck Collaboration XI (2014) over the same range in $N_{\rm H}$ (see their Fig. 20). On the other hand, for the $E(B-V)$ map from Green et al. (2015) we see a strong dependence of the ratio on $N_{\rm H}$, i.e. a lack of linearity between this measure of $E(B-V)$ and $N_{\rm H}$. The binned results

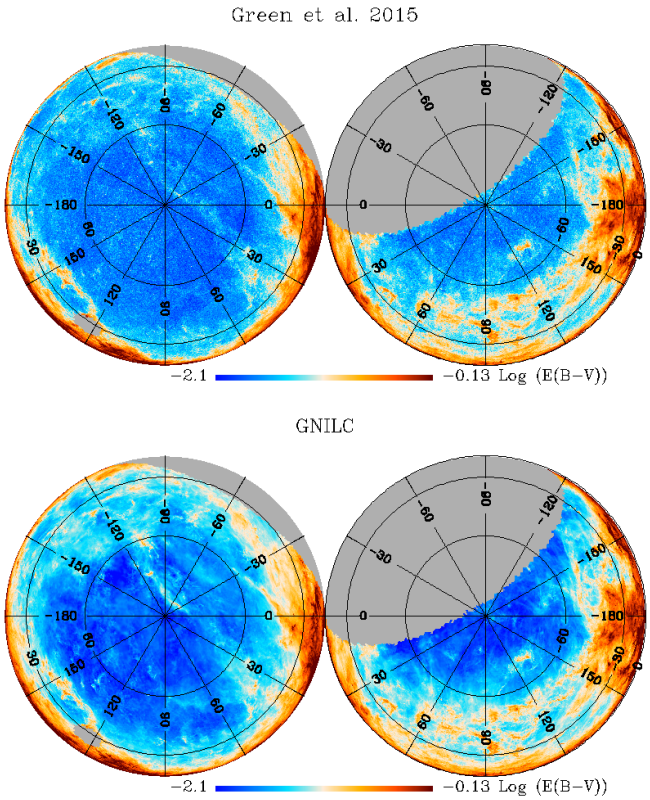

Fig. 18. Polar orthographic projections of the $E(B-V)$ maps at north (*left*) and south (*right*) Galactic poles in the Pan-STARRS 1 survey area (Onaka et al. 2008). *Top*: $E(B-V)$ map from Green et al. (2015). *Bottom*: GNILC $E(B-V)$ map.

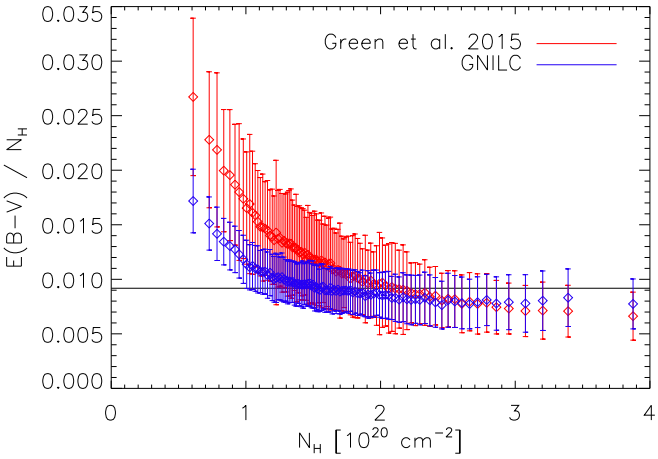

Fig. 19. T–T scatter plot between the ratio $E(B-V)/N_{\rm H}$ and the gas column density $N_{\rm H}$ for the two-dimensional projection of the $E(B-V)$ map of Green et al. (2015) (red diamonds) and the GNILC $E(B-V)$ map (blue diamonds) in the high-latitude region of the sky defined in Fig. 10. Each point is the average of $E(B-V)/N_{\rm H}$ values in a bin of $N_{\rm H}$. The bin size varies such that there is always the same number of samples per bin.

from the map of Green et al. (2015) also show a larger dispersion. From these three perspectives, the GNILC optical depth map appears to provide a better template for $E(B-V)$ studies. Both products show an excess ratio at the lowest column densities ($N_{\rm H} < 1 \times 10^{20}$ cm^{-2}); this could be the signature of dust mixed with ionized hydrogen, which is not traced by neutral H I emission (see discussion in Planck Collaboration XI 2014).

7. Conclusions

We have produced a significantly improved all-sky map of the Galactic thermal dust emission from the *Planck* data and the IRAS 100 μm map. We have fitted a modified blackbody model in each pixel to the GNILC dust maps produced at 353, 545, 857, and 3000 GHz. The new *Planck* GNILC dust model has been compared with the dust models P13 and P15 and has been shown to be significantly less contaminated by CIB and noise.

By exploiting the distinct signature of Galactic dust and extragalactic CIB angular power spectra, the GNILC method successfully separates the Galactic thermal dust emission from the CIB anisotropies in the *Planck* PR2 maps. We have reduced the dispersion due to CIB contamination of the estimated dust temperature and spectral index in the GNILC dust map with respect to the P13 dust map by a factor 1.3 for T on the whole sky (1.6 at high latitude) and a factor 2.1 for β on the whole sky (2.6 at high latitude). The GNILC dust map at 353 GHz has already been implemented as the thermal dust model in the released *Planck* simulations of the sky (Planck Collaboration XII 2016).

The GNILC method, presented in this work, also gives access to the CIB anisotropies over a large fraction of the sky. Within the small fields considered in Planck Collaboration XXX (2014), the GNILC CIB maps and the CIB 2013 maps are found to be consistent with a Pearson correlation coefficient larger than 0.8. The GNILC CIB maps can be very useful as indirect tracers of the dark matter over a large area of the sky and they are recommended for the investigation of cross-correlations with galaxy weak lensing data and other tracers of large-scale structure.

The new *Planck* GNILC products are made publicly available on the *Planck* Legacy Archive[3]. They include:

- the CIB-removed GNILC thermal dust maps at 353, 545, and 857 GHz;
- the GNILC CIB maps at 353, 545, and 857 GHz;
- the GNILC dust optical depth map;
- the GNILC dust spectral index map;
- the GNILC dust temperature map;
- the GNILC effective beam map for the thermal dust.

Acknowledgements. The Planck Collaboration acknowledges the support of: ESA; CNES, and CNRS/INSU-IN2P3-INP (France); ASI, CNR, and INAF (Italy); NASA and DoE (USA); STFC and UKSA (UK); CSIC, MINECO, JA, and RES (Spain); Tekes, AoF, and CSC (Finland); DLR and MPG (Germany); CSA (Canada); DTU Space (Denmark); SER/SSO (Switzerland); RCN (Norway); SFI (Ireland); FCT/MCTES (Portugal); ERC and PRACE (EU). A description of the Planck Collaboration and a list of its members, indicating which technical or scientific activities they have been involved in, can be found at http://www.cosmos.esa.int/web/planck/planck-collaboration. Some of the results in this paper have been derived using the HEALPix package. The research leading to these results has received funding from the ERC Grant No. 307209.

References

Akaike, H. 1974, IEEE Transactions on Automatic Control, 19, 716
Basak, S., & Delabrouille, J. 2012, MNRAS, 419, 1163
Basak, S., & Delabrouille, J. 2013, MNRAS, 435, 18
Bennett, C. L., Hill, R. S., Hinshaw, G., et al. 2003, ApJS, 148, 97
BICEP2/Keck Array and Planck Collaborations 2015, Phys. Rev. Lett., 114, 101301
Cardoso, J., Martin, M., Delabrouille, J., Betoule, M., & Patanchon, G. 2008, IEEE Journal of Selected Topics in Signal Processing, 2, 735

[3] http://pla.esac.esa.int/pla; see Release PR2 – 2015, Foreground maps, CIB or Dust.

Delabrouille, J., Cardoso, J.-F., & Patanchon, G. 2003, MNRAS, 346, 1089
Delabrouille, J., Cardoso, J., Le Jeune, M., et al. 2009, A&A, 493, 835
Delabrouille, J., Betoule, M., Melin, J.-B., et al. 2013, A&A, 553, A96
Draine, B. T., & Li, A. 2007, ApJ, 657, 810
Eriksen, H. K., Jewell, J. B., Dickinson, C., et al. 2008, ApJ, 676, 10
Gispert, R., Lagache, G., & Puget, J. L. 2000, A&A, 360, 1
Górski, K. M., Hivon, E., Banday, A. J., et al. 2005, ApJ, 622, 759
Green, G. M., Schlafly, E. F., Finkbeiner, D. P., et al. 2015, ApJ, 810, 25
Guilloux, F., Faÿ, G., & Cardoso, J.-F. 2009, Appl. Comput. Harmon. Anal., 26, 143
Isobe, T., Feigelson, E. D., Akritas, M. G., & Babu, G. J. 1990, ApJ, 364, 104
Kalberla, P. M. W., Burton, W. B., Hartmann, D., et al. 2005, A&A, 440, 775
Kelsall, T., Weiland, J. L., Franz, B. A., et al. 1998, ApJ, 508, 44
Kullback, S. 1968, Information theory and statistics (New York: Dover)
Lagache, G., Puget, J.-L., & Dole, H. 2005, ARA&A, 43, 727
Land, K., & Slosar, A. 2007, Phys. Rev. D, 76, 087301
Martin, P. G., Blagrave, K. P. M., Lockman, F. J., et al. 2015, ApJ, 809, 153
Miville-Deschênes, M.-A., & Lagache, G. 2005, ApJS, 157, 302
Narcowich, F., Petrushev, P., & Ward, J. 2006, SIAM J. Math. Anal., 38, 574
Olivari, L. C., Remazeilles, M., & Dickinson, C. 2016, MNRAS, 456, 2749
Onaka, P., Tonry, J. L., Isani, S., et al. 2008, Proc. SPIE, 7014, 70140D
Planck Collaboration XVIII. 2011, A&A, 536, A18
Planck Collaboration XIX. 2011, A&A, 536, A19
Planck Collaboration XI. 2014, A&A, 571, A11
Planck Collaboration XII. 2014, A&A, 571, A12
Planck Collaboration XIV. 2014, A&A, 571, A14
Planck Collaboration XV. 2014, A&A, 571, A15
Planck Collaboration XVIII. 2014, A&A, 571, A18
Planck Collaboration XXX. 2014, A&A, 571, A30
Planck Collaboration VI. 2016, A&A, 594, A6
Planck Collaboration VIII. 2016, A&A, 594, A8
Planck Collaboration X. 2016, A&A, 594, A10
Planck Collaboration XII. 2016, A&A, 594, A12
Planck Collaboration XXII. 2016, A&A, 594, A22
Planck Collaboration XXVI. 2016, A&A, 594, A26
Planck Collaboration Int. XVII. 2014, A&A, 566, A55
Planck Collaboration Int. XXVIII. 2015, A&A, 582, A31
Planck Collaboration Int. XXX. 2016, A&A, 586, A133
Planck Collaboration Int. XXXII. 2016, A&A, 586, A135
Puget, J.-L., Abergel, A., Bernard, J.-P., et al. 1996, A&A, 308, L5
Remazeilles, M., Delabrouille, J., & Cardoso, J.-F. 2011a, MNRAS, 410, 2481
Remazeilles, M., Delabrouille, J., & Cardoso, J.-F. 2011b, MNRAS, 418, 467
Remazeilles, M., Aghanim, N., & Douspis, M. 2013, MNRAS, 430, 370
Remazeilles, M., Dickinson, C., Banday, A. J., Bigot-Sazy, M.-A., & Ghosh, T. 2015, MNRAS, 451, 4311
Remazeilles, M., Dickinson, C., Eriksen, H. K. K., & Wehus, I. K. 2016, MNRAS, 458, 2032
Riess, A. G., Press, W. H., & Kirshner, R. P. 1996, ApJ, 473, 588
Savage, B. D., & Jenkins, E. B. 1972, ApJ, 172, 491
Schlegel, D. J., Finkbeiner, D. P., & Davis, M. 1998, ApJ, 500, 525
Serra, P., Lagache, G., Doré, O., Pullen, A., & White, M. 2014, A&A, 570, A98

[1] APC, AstroParticule et Cosmologie, Université Paris Diderot, CNRS/IN2P3, CEA/lrfu, Observatoire de Paris, Sorbonne Paris Cité, 10 rue Alice Domon et Léonie Duquet, 75205 Paris Cedex 13, France
[2] African Institute for Mathematical Sciences, 6-8 Melrose Road, Muizenberg 7945, Cape Town, South Africa
[3] Agenzia Spaziale Italiana Science Data Center, via del Politecnico snc, 00133 Roma, Italy
[4] Astrophysics Group, Cavendish Laboratory, University of Cambridge, J J Thomson Avenue, Cambridge CB3 0HE, UK
[5] Astrophysics & Cosmology Research Unit, School of Mathematics, Statistics & Computer Science, University of KwaZulu-Natal, Westville Campus, Private Bag X54001, Durban 4000, South Africa
[6] CITA, University of Toronto, 60 St. George St., Toronto, ON M5S 3H8, Canada
[7] CNRS, IRAP, 9 Av. colonel Roche, BP 44346, 31028 Toulouse Cedex 4, France
[8] California Institute of Technology, Pasadena, California, CA 91125, USA
[9] Computational Cosmology Center, Lawrence Berkeley National Laboratory, Berkeley, California, CA 94720, USA
[10] DTU Space, National Space Institute, Technical University of Denmark, Elektrovej 327, 2800 Kgs. Lyngby, Denmark
[11] Département de Physique Théorique, Université de Genève, 24 Quai E. Ansermet, 1211 Genève 4, Switzerland
[12] Departamento de Astrofísica, Universidad de La Laguna (ULL), 38206 La Laguna, Tenerife, Spain
[13] Departamento de Física, Universidad de Oviedo, Avda. Calvo Sotelo s/n, 33007 Oviedo, Spain
[14] Department of Astrophysics/IMAPP, Radboud University Nijmegen, PO Box 9010, 6500 GL Nijmegen, The Netherlands
[15] Department of Physics & Astronomy, University of British Columbia, 6224 Agricultural Road, Vancouver, British Columbia, Canada
[16] Department of Physics and Astronomy, Dana and David Dornsife College of Letter, Arts and Sciences, University of Southern California, Los Angeles, CA 90089, USA
[17] Department of Physics and Astronomy, University College London, London WC1E 6BT, UK
[18] Department of Physics and Astronomy, University of Sussex, Brighton BN1 9QH, UK
[19] Department of Physics, Gustaf Hällströmin katu 2a, University of Helsinki, 00014 Helsinki, Finland
[20] Department of Physics, Princeton University, Princeton, New Jersey, NJ 08544, USA
[21] Department of Physics, University of California, Santa Barbara, California, CA 93106, USA
[22] Department of Physics, University of Illinois at Urbana-Champaign, 1110 West Green Street, Urbana, Illinois, USA
[23] Dipartimento di Fisica e Astronomia G. Galilei, Università degli Studi di Padova, via Marzolo 8, 35131 Padova, Italy
[24] Dipartimento di Fisica e Astronomia, Alma Mater Studiorum, Università degli Studi di Bologna, Viale Berti Pichat 6/2, 40127 Bologna, Italy
[25] Dipartimento di Fisica e Scienze della Terra, Università di Ferrara, via Saragat 1, 44122 Ferrara, Italy
[26] Dipartimento di Fisica, Università La Sapienza, P. le A. Moro 2, 00185 Roma, Italy
[27] Dipartimento di Fisica, Università degli Studi di Milano, via Celoria 16, 20133 Milano, Italy
[28] Dipartimento di Fisica, Università degli Studi di Trieste, via A. Valerio 2, 34127 Trieste, Italy
[29] Dipartimento di Fisica, Università di Roma Tor Vergata, via della Ricerca Scientifica 1, Roma, Italy
[30] Dipartimento di Matematica, Università di Roma Tor Vergata, Via della Ricerca Scientifica, 1, 00133 Roma, Italy
[31] European Space Agency, ESAC, Planck Science Office, Camino bajo del Castillo, s/n, Urbanización Villafranca del Castillo, 28692 Villanueva de la Cañada, Madrid, Spain
[32] European Space Agency, ESTEC, Keplerlaan 1, 2201 AZ Noordwijk, The Netherlands
[33] Gran Sasso Science Institute, INFN, viale F. Crispi 7, 67100 L'Aquila, Italy
[34] HGSFP and University of Heidelberg, Theoretical Physics Department, Philosophenweg 16, 69120 Heidelberg, Germany
[35] Helsinki Institute of Physics, Gustaf Hällströmin katu 2, University of Helsinki, 00014 Helsinki, Finland
[36] INAF–Osservatorio Astronomico di Padova, Vicolo dell'Osservatorio 5, 35122 Padova, Italy
[37] INAF–Osservatorio Astronomico di Roma, via di Frascati 33, 00040 Monte Porzio Catone, Italy
[38] INAF–Osservatorio Astronomico di Trieste, via G.B. Tiepolo 11, 40127 Trieste, Italy
[39] INAF/IASF Bologna, via Gobetti 101, 40129 Bologna, Italy
[40] INAF/IASF Milano, via E. Bassini 15, 20133 Milano, Italy
[41] INFN – CNAF, viale Berti Pichat 6/2, 40127 Bologna, Italy
[42] INFN, Sezione di Bologna, viale Berti Pichat 6/2, 40127 Bologna, Italy
[43] INFN, Sezione di Ferrara, via Saragat 1, 44122 Ferrara, Italy
[44] INFN, Sezione di Roma 1, Università di Roma Sapienza, Piazzale Aldo Moro 2, 00185 Roma, Italy
[45] INFN, Sezione di Roma 2, Università di Roma Tor Vergata, via della Ricerca Scientifica 1, 00185 Roma, Italy

[46] Imperial College London, Astrophysics group, Blackett Laboratory, Prince Consort Road, London, SW7 2AZ, UK
[47] Institut d'Astrophysique Spatiale, CNRS, Univ. Paris-Sud, Université Paris-Saclay, Bât. 121, 91405 Orsay Cedex, France
[48] Institut d'Astrophysique de Paris, CNRS (UMR 7095), 98 bis Boulevard Arago, 75014 Paris, France
[49] Institute of Astronomy, University of Cambridge, Madingley Road, Cambridge CB3 0HA, UK
[50] Institute of Theoretical Astrophysics, University of Oslo, Blindern, 0371 Oslo, Norway
[51] Instituto de Astrofísica de Canarias, C/Vía Láctea s/n, La Laguna, 38205 Tenerife, Spain
[52] Instituto de Física de Cantabria (CSIC-Universidad de Cantabria), Avda. de los Castros s/n, 39005 Santander, Spain
[53] Istituto Nazionale di Fisica Nucleare, Sezione di Padova, via Marzolo 8, 35131 Padova, Italy
[54] Jet Propulsion Laboratory, California Institute of Technology, 4800 Oak Grove Drive, Pasadena, California, CA 31109, USA
[55] Jodrell Bank Centre for Astrophysics, Alan Turing Building, School of Physics and Astronomy, The University of Manchester, Oxford Road, Manchester, M13 9PL, UK
[56] Kavli Institute for Cosmological Physics, University of Chicago, Chicago, IL 60637, USA
[57] Kavli Institute for Cosmology Cambridge, Madingley Road, Cambridge, CB3 0HA, UK
[58] LAL, Université Paris-Sud, CNRS/IN2P3, 91898 Orsay, France
[59] LERMA, CNRS, Observatoire de Paris, 61 Avenue de l'Observatoire, 75014 Paris, France
[60] Laboratoire Traitement et Communication de l'Information, CNRS (UMR 5141) and Télécom ParisTech, 46 rue Barrault, 75634 Paris Cedex 13, France
[61] Laboratoire de Physique Subatomique et Cosmologie, Université Grenoble-Alpes, CNRS/IN2P3, 53 rue des Martyrs, 38026 Grenoble Cedex, France
[62] Laboratoire de Physique Théorique, Université Paris-Sud 11 & CNRS, Bâtiment 210, 91405 Orsay, France
[63] Lawrence Berkeley National Laboratory, Berkeley, California, USA
[64] Max-Planck-Institut für Astrophysik, Karl-Schwarzschild-Str. 1, 85741 Garching, Germany
[65] Mullard Space Science Laboratory, University College London, Surrey RH5 6NT, UK
[66] Nicolaus Copernicus Astronomical Center, Bartycka 18, 00-716 Warsaw, Poland
[67] Nordita (Nordic Institute for Theoretical Physics), Roslagstullsbacken 23, 106 91 Stockholm, Sweden
[68] SISSA, Astrophysics Sector, via Bonomea 265, 34136 Trieste, Italy
[69] School of Chemistry and Physics, University of KwaZulu-Natal, Westville Campus, Private Bag X54001, Durban 4000, South Africa
[70] School of Physics and Astronomy, Cardiff University, Queens Buildings, The Parade, Cardiff, CF24 3AA, UK
[71] School of Physics and Astronomy, University of Nottingham, Nottingham NG7 2RD, UK
[72] Simon Fraser University, Department of Physics, 8888 University Drive, Burnaby BC, Canada
[73] Sorbonne Université-UPMC, UMR 7095, Institut d'Astrophysique de Paris, 98 bis Boulevard Arago, 75014 Paris, France
[74] Space Sciences Laboratory, University of California, Berkeley, California, CA 94720, USA
[75] Sub-Department of Astrophysics, University of Oxford, Keble Road, Oxford OX1 3RH, UK
[76] The Oskar Klein Centre for Cosmoparticle Physics, Department of Physics, Stockholm University, AlbaNova, 106 91 Stockholm, Sweden
[77] UPMC Univ Paris 06, UMR 7095, 98 bis Boulevard Arago, 75014 Paris, France
[78] Université de Toulouse, UPS-OMP, IRAP, 31028 Toulouse Cedex 4, France
[79] University of Granada, Departamento de Física Teórica y del Cosmos, Facultad de Ciencias, 18071 Granada, Spain
[80] Warsaw University Observatory, Aleje Ujazdowskie 4, 00-478 Warszawa, Poland

Appendix A: Description of the GNILC method

The generalized needlet internal linear combination, GNILC (Remazeilles et al. 2011b), is a component-separation method designed to reconstruct the diffuse emission of a complex component originating from multiple correlated sources of emission, such as the Galactic foreground emission or the cosmic infrared background radiation.

GNILC is a multi-dimensional generalization (Sect. A.1) of the standard internal linear combination (ILC) method, which has been extensively used to reconstruct one-dimensional components such as the CMB emission (Bennett et al. 2003; Planck Collaboration XII 2014) or the Sunyaev-Zeldovich (SZ) signal (Remazeilles et al. 2013; Planck Collaboration XXII 2016). A two-dimensional extension of the ILC, the so-called Constrained ILC, was first developed by Remazeilles et al. (2011a) to reconstruct both maps of the CMB and the SZ components, with vanishing contamination from one into the other. GNILC is a further generalization in which the dimension of the ILC filter, which is related to the dimension of the signal subspace, is no longer fixed, but varies with both the direction in the sky and the angular scale, depending on the effective local signal-to-noise ratio, i.e. the local conditions of contamination in both real space and harmonic space.

In this work, the signal is Galactic and the noise contributions consist of the CIB, the CMB, and the instrumental noise. The effective signal-to-noise ratio is determined locally both over the sky and over different angular scales by decomposing the data onto a wavelet (needlet) frame and by making use of a prior on the CIB power spectrum (Sect. A.2). The dimension of the Galactic signal is estimated locally in each wavelet domain through a modified principal component analysis (PCA) constrained by the power spectrum of the CIB (Sect. A.3). The effective dimension of the Galactic subspace, given by the local number of principal components, is not determined ad hoc but through a statistical model selection by the Akaike Information Criterion (Sect. A.4). The prior of the CIB power spectrum is only used at the stage of determining the number of principal components, i.e. the dimension of the Galactic signal subspace. There is no prior assumption about the Galactic signal.

A.1. Multi-dimensional internal linear combination

We model the sky observation, $x_i(p)$, at frequency channel i and in the direction p in the sky (pixel), as the combination of the Galactic foreground emission, the CIB emission, the CMB emission, and the instrumental noise:

$$x_i(p) = f_i(p) + s_i^{\rm CIB}(p) + a_i s^{\rm CMB}(p) + n_i(p), \tag{A.1}$$

assuming no correlations between the different components of emission. Equation (A.1) can be recast in the $N_{\rm ch}\times 1$ vector form, where $N_{\rm ch}$ is the number of frequency channels:

$$\boldsymbol{x}(p) = \boldsymbol{f}(p) + \boldsymbol{s}^{\rm CIB}(p) + \boldsymbol{a}\, s^{\rm CMB}(p) + \boldsymbol{n}(p), \tag{A.2}$$

Here $\boldsymbol{x} = (x_i)_{1\le i\le N_{\rm ch}}$ collects the $N_{\rm ch}$ observation maps, each of them being a mixture of the Galactic foreground emission, $\boldsymbol{f}$ (i.e. the thermal dust emission at high frequencies), the CIB emission, $\boldsymbol{s}^{\rm CIB}(p)$, the CMB emission, $s^{\rm CMB}(p)$, scaling with a known spectral distribution, $\boldsymbol{a}$, and the instrumental noise, $\boldsymbol{n}$.

The $N_{\rm ch}\times N_{\rm ch}$ frequency-frequency covariance matrix of the sky observations, $\mathsf{R}(p) = (\mathsf{R}_{ij}(p))_{1\le i,j\le N_{\rm ch}} = \langle \boldsymbol{x}(p)\boldsymbol{x}(p)^{\mathsf{T}}\rangle$, is

$$\mathsf{R} = \mathsf{R}_f + \mathsf{R}_{\rm CIB} + \mathsf{R}_{\rm CMB} + \mathsf{R}_{\rm noise} \tag{A.3}$$

where $\mathsf{R}_f = \langle \boldsymbol{f}\boldsymbol{f}^{\mathsf{T}}\rangle$ is the covariance matrix of the Galactic signal, $\mathsf{R}_{\rm CIB} = \langle \boldsymbol{s}^{\rm CIB}\left(\boldsymbol{s}^{\rm CIB}\right)^{\mathsf{T}}\rangle$ the covariance matrix of the CIB, $\mathsf{R}_{\rm CMB} = \langle \left(s^{\rm CMB}\right)^2\rangle \boldsymbol{a}\boldsymbol{a}^{\mathsf{T}}$ the covariance matrix of the CMB, and $\mathsf{R}_{\rm noise} = \langle \boldsymbol{n}\boldsymbol{n}^{\mathsf{T}}\rangle$ the covariance matrix of the noise.

The Galactic foreground signal, $\boldsymbol{f}$, is a complex multi-component emission emanating from various physical processes (e.g., thermal dust emission, synchrotron emission, and free-free emission) with spectral properties varying over the sky. The number of degrees of freedom of the Galactic foreground signal would be infinite in the case of an infinitely narrow beam. However, in practice the beam is finite and the observations are limited by the number of frequency channels and the level of noise so that the effective number of Galactic degrees of freedom required to describe the Galactic emission is finite. In addition, the various physical components of the diffuse Galactic emission are correlated, therefore the Galactic signal, $\boldsymbol{f}$, can be represented as the superposition of a relatively small number, m, of independent (not physical) templates, $\boldsymbol{t}$:

$$\boldsymbol{f} = \mathsf{F}\boldsymbol{t}, \tag{A.4}$$

where F is an $N_{\rm ch}\times m$ mixing matrix giving the contribution from the templates in each frequency channel. Therefore, the covariance matrix of the Galactic signal is an $N_{\rm ch}\times N_{\rm ch}$ matrix of rank m:

$$\mathsf{R}_f = \mathsf{F}\mathsf{R}_t\mathsf{F}^{\mathsf{T}} \tag{A.5}$$

where $\mathsf{R}_t = \langle \boldsymbol{t}\boldsymbol{t}^{\mathsf{T}}\rangle$ is a full-rank $m\times m$ matrix.

We now address the problem of estimating the set of maps, $\boldsymbol{f}(p)$, i.e. determining a "catch-all" foreground component comprising the emission of the diffuse Galactic interstellar medium. The objective is to construct estimated maps, $\widehat{\boldsymbol{f}}(p)$, which are good matches to what would be observed by the instrument in the absence of CMB, CIB, and noise.

For extracting such an emission component from multi-frequency observations, we propose to generalize the internal linear combination (ILC) method to address the case of such a "multi-dimensional component" (m–dimensional, with $m < N_{\rm ch}$). We consider the estimation of $\boldsymbol{f}$ by a weighted linear operation

$$\widehat{\boldsymbol{f}} = \mathsf{W}\boldsymbol{x}, \tag{A.6}$$

where the $N_{\rm ch}\times N_{\rm ch}$ weight matrix, W, is designed to offer unit response to the Galactic foreground emission while minimizing the total variance of the vector estimate $\widehat{\boldsymbol{f}}$. Stated otherwise, the matrix W is the minimizer of $E(\|\mathsf{W}\boldsymbol{x}\|^2)$ under the constraint $\mathsf{W}\mathsf{F} = \mathsf{F}$. The weights matrix, W, thus solves the following constrained variance minimization problem

$$\min_{\mathsf{W}\mathsf{F}=\mathsf{F}} \mathrm{Tr}\left(\mathsf{W}\widehat{\mathsf{R}}\mathsf{W}^{\mathsf{T}}\right), \tag{A.7}$$

where $\widehat{\mathsf{R}}$ is the covariance matrix of the observations, $\boldsymbol{x}$. This problem can be solved by introducing a Lagrange multiplier matrix, Λ, and the Lagrangian

$$\mathcal{L}(\mathsf{W},\Lambda) = \mathrm{Tr}\left(\mathsf{W}\widehat{\mathsf{R}}\mathsf{W}^{\mathsf{T}}\right) - \mathrm{Tr}\left(\Lambda^{\mathsf{T}}(\mathsf{W}\mathsf{F}-\mathsf{F})\right). \tag{A.8}$$

By differentiating Eq. (A.8) with respect to W, one finds that $\partial\mathcal{L}(\mathsf{W},\Lambda)/\partial\mathsf{W} = 0$ is solved by

$$2\mathsf{W}\widehat{\mathsf{R}} = \Lambda\mathsf{F}^{\mathsf{T}}. \tag{A.9}$$

By imposing the constraint $\mathsf{WF} = \mathsf{F}$ on Eq. (A.9), one then finds that $\Lambda = 2\mathsf{F}(\mathsf{F}^{\mathsf{T}}\widehat{\mathsf{R}}^{-1}\mathsf{F})^{-1}$. Hence, the solution of the Eq. (A.7) is given by the ILC weight matrix

$$\mathsf{W} = \mathsf{F}\left(\mathsf{F}^{\mathsf{T}}\widehat{\mathsf{R}}^{-1}\mathsf{F}\right)^{-1}\mathsf{F}^{\mathsf{T}}\widehat{\mathsf{R}}^{-1}. \tag{A.10}$$

Multi-dimensional ILC appears as a direct generalization of the one-dimensional ILC of Bennett et al. (2003). The mixing matrix, F, of the Galactic signal and its dimension, m, are the unknowns of the problem. However, it is important to notice that expression (A.10) for W is invariant if F is changed into FT for any invertible matrix T. Hence, implementing the multi-dimensional ILC filter (A.10) only requires that the foreground mixing matrix, F, be known up to right multiplication by an invertible factor (Remazeilles et al. 2011b). In other words, the only meaningful and mandatory quantity for implementing a multi-dimensional ILC is not the "true" mixing matrix but the column space of F, i.e. the dimension, m, of the Galactic signal subspace. This is the purpose of the Sects. A.3 and A.4.

The frequency-frequency covariance matrix of the observations, R, can be estimated from the observation maps across the frequency channels. The coefficients of the covariance matrix of the observations for the pair of frequencies (a, b) is computed empirically as follows:

$$\widehat{\mathsf{R}}_{ab}(p) = \sum_{p' \in \mathcal{D}(p)} x_a(p')\, x_b(p'), \tag{A.11}$$

where $\mathcal{D}(p)$ is a domain of pixels centred around the pixel p. In this work, the pixel domain, $\mathcal{D}(p)$, is defined by smoothing the product map $x_i(p)\, x_j(p)$ with a Gaussian window in pixel space.

A.2. Nuisance covariance matrix

We define the "nuisance" covariance matrix, $\mathsf{R}_{\rm N}$, as the sum of the CIB covariance matrix, the CMB covariance matrix, and the noise covariance matrix:

$$\mathsf{R}_{\rm N} = \mathsf{R}_{\rm CIB} + \mathsf{R}_{\rm CMB} + \mathsf{R}_{\rm noise}. \tag{A.12}$$

Therefore,

$$\mathsf{R} = \mathsf{R}_f + \mathsf{R}_{\rm N}. \tag{A.13}$$

Our aim is to obtain an estimate, $\widehat{\mathsf{R}}_{\rm N}$, of the nuisance covariance matrix. In combination with the estimate of the full covariance matrix, $\widehat{\mathsf{R}}$ (Eq. (A.11)), the nuisance covariance matrix, $\widehat{\mathsf{R}}_{\rm N}$, allows us to constrain the Galactic signal subspace.

The noise covariance matrix, $\mathsf{R}_{\rm noise}$, can be estimated from the covariance of the half-difference maps between the HM1 and the HM2 half-mission surveys of *Planck* (Planck Collaboration VIII 2016), since the sky emission cancels out in the difference while the noise does not. The half-difference map for frequency channel a is

$$n_a(p) = \frac{x_a^{HM1}(p) - x_a^{HM2}(p)}{2}, \tag{A.14}$$

where x_a^{HM1} and x_a^{HM2} are the *Planck* HM1 map and the *Planck* HM2 map, respectively. Similarly to the full covariance matrix in Eq. (A.11), the noise covariance matrix is then estimated empirically:

$$\left(\widehat{\mathsf{R}}_{\rm noise}\right)_{ab}(p) = \sum_{p' \in \mathcal{D}(p)} n_a(p')\, n_b(p'). \tag{A.15}$$

The *Planck* CMB best-fit ΛCDM model C_ℓ (Planck Collaboration XV 2014) and the *Planck* CIB best-fit $C_\ell^{a\times b}$ models (Planck Collaboration XXX 2014) are used as priors to estimate: (i) the CMB covariance matrix, $\mathsf{R}_{\rm CMB}$; and (ii) the CIB covariance matrix, $\mathsf{R}_{\rm CIB}$, in pixel space.

We first simulate a Gaussian CMB map, $\widetilde{y}(p)$, having a power spectrum given by the *Planck* CMB best-fit C_ℓ, and we scale it across frequencies through the known CMB spectral distribution, $\boldsymbol{a}$. In harmonic space, the cross-power spectrum of the simulated CMB maps is given by

$$\langle a_a \widetilde{y}_{\ell m} a_b \widetilde{y}^*_{\ell m}\rangle = C_\ell a_a a_b, \tag{A.16}$$

where C_ℓ is the *Planck* CMB best-fit. From the simulated CMB maps, $\boldsymbol{a}\widetilde{y}(p)$, we are able to compute the CMB covariance matrix in pixel space, $\widehat{\mathsf{R}}_{\rm CMB}(p)$, in the same way as in Eqs. (A.11) and (A.15).

From the *Planck* CIB best-fit cross-and auto-power spectra, $C_{\rm CIB}^{a\times b}(\ell)$, we simulate $N_{\rm ch}$ correlated Gaussian maps[4], $\widetilde{z}_a(p)$, having a correlation matrix in harmonic space given by

$$\langle \widetilde{z}_a(\ell, m)\widetilde{z}^*_b(\ell, m)\rangle = C_{\rm CIB}^{a\times b}(\ell), \tag{A.17}$$

where $C_{\rm CIB}^{a\times b}(\ell)$ are the *Planck* CIB best-fits. From the simulated correlated CIB maps, $\widetilde{z}_a(p)$, we can compute the CIB covariance matrix in pixel space, $\widehat{\mathsf{R}}_{\rm CIB}(p)$, in the same way as in Eqs. (A.11) and (A.15). For all $a, b < 143$ GHz, the coefficients of $\widehat{\mathsf{R}}_{{\rm CIB}\ ab}$ are set to zero because there is no *Planck* measurement of the CIB at those low frequencies, and therefore they are considered negligible.

A.3. Determining the Galactic signal subspace with a constrained PCA

Once both the observation covariance matrix, $\widehat{\mathsf{R}}$, and the nuisance covariance matrix, $\widehat{\mathsf{R}}_{\rm N}$, have been computed, we can "whiten" the *Planck* data by making the transformation

$$\boldsymbol{x} \leftarrow \widehat{\mathsf{R}}_{\rm N}^{-1/2}\boldsymbol{x}, \tag{A.18}$$

such that the covariance matrix of the transformed *Planck* observations is now given by

$$\widehat{\mathsf{R}}_{\rm N}^{-1/2}\mathsf{R}\widehat{\mathsf{R}}_{\rm N}^{-1/2}. \tag{A.19}$$

Assuming that the prior CIB covariance matrix, $\widehat{\mathsf{R}}_{\rm CIB}$, is close the real CIB covariance matrix, $\mathsf{R}_{\rm CIB}$, we have that

$$\widehat{\mathsf{R}}_{\rm N}^{-1/2}\mathsf{R}_{\rm N}\widehat{\mathsf{R}}_{\rm N}^{-1/2} \approx \mathsf{I}, \tag{A.20}$$

where I is the identity matrix. In this way, from Eq. (A.13) the covariance matrix of the transformed *Planck* observations becomes

$$\widehat{\mathsf{R}}_{\rm N}^{-1/2}\mathsf{R}\widehat{\mathsf{R}}_{\rm N}^{-1/2} \approx \widehat{\mathsf{R}}_{\rm N}^{-1/2}\mathsf{R}_f\widehat{\mathsf{R}}_{\rm N}^{-1/2} + \mathsf{I}, \tag{A.21}$$

such that the power of all the nuisance contamination, including CIB, CMB, and noise, is encoded in the matrix I, which is close to an identity matrix. Typically, the coefficients of the transformed observation covariance matrix (Eq. (A.21)) provide

[4] It could be argued that the non-Gaussianity of the CIB anisotropies should be taken into account in the statistics, in order to make the separation of Galactic foregrounds and CIB more accurate. However, the non-Gaussianity of the CIB is negligible compared to the non-Gaussianity of the Galactic foregrounds, so that Gaussian statistics is a sufficient approximation for separating the thermal dust and the CIB.

the signal-to-noise ratio over the sky, i.e. the power of the Galactic signal divided by the overall power of the CIB-plus-CMB-plus-noise.

Therefore, by diagonalizing the transformed observation covariance matrix (Eq. (A.21)), we obtain the following eigenstructure:

$$\widehat{\mathsf{R}}_{\rm N}^{-1/2}\widehat{\widetilde{\mathsf{R}}}\widehat{\mathsf{R}}_{\rm N}^{-1/2} = \left[\mathsf{U}_{\rm S}\middle|\mathsf{U}_{\rm N}\right]\cdot\left[\begin{array}{c|c}\lambda_1+1 & \\ \cdots & \\ & \lambda_m+1\\ \hline & \mathsf{I}\end{array}\right]\cdot\left[\begin{array}{c}\mathsf{U}_{\rm S}^{\mathsf{T}}\\ \hline \mathsf{U}_{\rm N}^{\mathsf{T}}\end{array}\right]. \tag{A.22}$$

In such a representation, the eigenvalues of the covariance matrix $\widehat{\mathsf{R}}_{\rm N}^{-1/2}\widehat{\widetilde{\mathsf{R}}}\widehat{\mathsf{R}}_{\rm N}^{-1/2}$ that are close to unity do not contain any relevant power of the Galactic signal and the signal is dominated by the CIB, the CMB, and the noise. The corresponding eigenvectors span the nuisance subspace characterized by the number of degrees of freedom, $N_{\rm d.o.f.}$, of the CIB plus CMB plus noise only. Conversely, the subset of eigenvectors collected in the $N_{\rm ch}\times m$ matrix $\mathsf{U}_{\rm S}$, for which the eigenvalues of $\widehat{\mathsf{R}}_{\rm N}^{-1/2}\widehat{\widetilde{\mathsf{R}}}\widehat{\mathsf{R}}_{\rm N}^{-1/2}$ significantly depart from unity, span the Galactic signal subspace (principal components). The number of eigenvalues, m, that are much larger than unity corresponds to the dimension of the Galactic signal subspace, i.e. the number of independent (unphysical) templates contributing to the Galactic signal. This is a constrained principal component analysis (PCA), in the sense that the PCA is driven by the local signal-to-noise ratio.

The diagonalization of the transformed *Planck* covariance matrix of Eq. (A.22) can be written in a compact form as

$$\widehat{\mathsf{R}}_{\rm N}^{-1/2}\widehat{\widetilde{\mathsf{R}}}\widehat{\mathsf{R}}_{\rm N}^{-1/2} = \mathsf{U}_{\rm S}\mathsf{D}_{\rm S}\mathsf{U}_{\rm S}^{\mathsf{T}} + \mathsf{U}_{\rm N}\mathsf{U}_{\rm N}^{\mathsf{T}}, \tag{A.23}$$

where

$$\mathsf{D}_{\rm S} = {\rm diag}[\lambda_1+1, ..., \lambda_m+1] \tag{A.24}$$

is a $m\times m$ diagonal matrix and $[\mathsf{U}_{\rm S}|\mathsf{U}_{\rm N}]$ is an $N_{\rm ch}\times N_{\rm ch}$ orthonormal matrix collecting all the eigenvectors of $\widehat{\mathsf{R}}_{\rm N}^{-1/2}\widehat{\widetilde{\mathsf{R}}}\widehat{\mathsf{R}}_{\rm N}^{-1/2}$. Using Eq. (A.23) and the orthonormality condition, $\mathsf{U}_{\rm S}\mathsf{U}_{\rm S}^{\mathsf{T}} + \mathsf{U}_{\rm N}\mathsf{U}_{\rm N}^{\mathsf{T}} = \mathsf{I}$, the covariance matrix of the Galactic signal can be written as

$$\begin{aligned}\widehat{\mathsf{R}}_f &= \widehat{\widetilde{\mathsf{R}}} - \widehat{\mathsf{R}}_{\rm N}\\ &= \widehat{\mathsf{R}}_{\rm N}^{1/2}\left(\widehat{\mathsf{R}}_{\rm N}^{-1/2}\widehat{\widetilde{\mathsf{R}}}\widehat{\mathsf{R}}_{\rm N}^{-1/2} - \mathsf{I}\right)\widehat{\mathsf{R}}_{\rm N}^{1/2}\\ &= \widehat{\mathsf{R}}_{\rm N}^{1/2}\left(\mathsf{U}_{\rm S}\left(\mathsf{D}_{\rm S}-\mathsf{I}\right)\mathsf{U}_{\rm S}^{\mathsf{T}}\right)\widehat{\mathsf{R}}_{\rm N}^{1/2}.\end{aligned} \tag{A.25}$$

This is the power that "best matches" what would be observed by the instrument in the absence of CIB, CMB, and noise. Therefore, we estimate the Galactic signal, $\boldsymbol{f}$, by

$$\widehat{\boldsymbol{f}}(p) = \widehat{\mathsf{F}}\,\boldsymbol{t}, \tag{A.26}$$

where

$$\widehat{\mathsf{F}} = \widehat{\mathsf{R}}_{\rm N}^{1/2}\mathsf{U}_{\rm S} \tag{A.27}$$

is an $N_{\rm ch}\times m$ mixing matrix estimate, and $\boldsymbol{t}$ is an $m\times 1$ vector of independent templates whose covariance matrix is given by

$$\widehat{\mathsf{R}}_t = \mathsf{D}_{\rm S} - \mathsf{I}. \tag{A.28}$$

The estimate, $\widehat{\mathsf{F}}$, is the only useful information for implementing the multi-dimensional ILC filter of Eq. (A.10). It can be different from the true mixing matrix, F, of the Galactic signal as long as the column space is the same: let T be some invertible $m\times m$ matrix and consider the transformed matrices $\widetilde{\mathsf{F}} = \widehat{\mathsf{F}}\mathsf{T}^{-1}$ and $\widetilde{\mathsf{R}}_t = \mathsf{T}\widehat{\mathsf{R}}_t\mathsf{T}^{\mathsf{T}}$. These transformed matrices are an alternate factorization of the covariance matrix of the Galactic signal, $\widehat{\mathsf{R}}_f$, but they are equivalent, since by construction, $\widetilde{\mathsf{F}}\widetilde{\mathsf{R}}_t\widetilde{\mathsf{F}}^{\mathsf{T}} = \widehat{\mathsf{F}}\widehat{\mathsf{R}}_t\widehat{\mathsf{F}}^{\mathsf{T}}$. The ILC weights of Eq. (A.10) are unchanged under right multiplication by an invertible matrix. Therefore, the m independent templates, $\boldsymbol{t}$, can be replaced by any other linear combination, $\mathsf{T}\boldsymbol{t}$, as long as we are interested in reconstructing the overall Galactic signal, $\boldsymbol{f}$.

The number, m, of principal components in Eq. (A.22), or the effective dimension of the Galactic signal subspace, can vary over the sky, depending on the local signal-to-noise ratio. In particular, at high Galactic latitudes this number decreases because the contributions of the CIB, the CMB, and the noise starts dominating the Galactic signal (Fig. A.1). The dimension of the Galactic signal subspace is also expected to vary with angular scale because at small angular scales the power of the Galactic signal becomes dominated by the power of the noise and the CIB. Therefore, for the accurate separation of the Galactic and CIB signals we find it useful to estimate the dimension of the Galactic subspace locally both in space and in scale. This is achieved by decomposing the data on a wavelet frame.

In this work, the analysis is performed on a needlet frame (see, e.g., Delabrouille et al. 2009; Remazeilles et al. 2013 for the use of needlets in component separation). Basically, the spherical harmonic transforms of the maps, $a_{\ell m}$, are bandpass filtered in harmonic space, then transformed back into real space, therefore conserving a specific range of angular scales in the map. The result is called a needlet map, characterized by a given range of angular scales. The multi-dimensional ILC Eq. (A.6) is performed on the needlet maps independently for each range of scale, and the synthesized map is obtained by co-adding the ILC estimates at the various scales. The wavelet decomposition allows for estimating the dimension, m, of the Galactic signal subspace locally over the sky and over the angular scales, depending on the local conditions of contamination. In this work, the needlet bandpass windows (Fig. A.2) are defined in harmonic space from the difference of successive Gaussian beam transfer functions:

$$\begin{aligned}h^{(1)}(\ell) &= \sqrt{b_1(\ell)^2},\\ h^{j}(\ell) &= \sqrt{b_{j+1}(\ell)^2 - b_j(\ell)^2},\\ h^{(10)}(\ell) &= \sqrt{1-b_{10}(\ell)^2},\end{aligned} \tag{A.29}$$

where

$$b_j(\ell) = \exp\left(-\ell(\ell+1)\sigma_j^2/2\right) \tag{A.30}$$

and

$$\sigma_j = \left(\frac{1}{\sqrt{8\ln 2}}\right)\left(\frac{\pi}{180\times 60}\right)FWHM[j] \tag{A.31}$$

with $FWHM = [300', 120', 60', 45', 30', 15', 10', 7.5', 5']$. In this way we have

$$\sum_{j=1}^{10}\left(h^j(\ell)\right)^2 = 1, \tag{A.32}$$

such that there is no effective filtering of any power at any scale in the final maps synthesized from the different needlet scales after component separation.

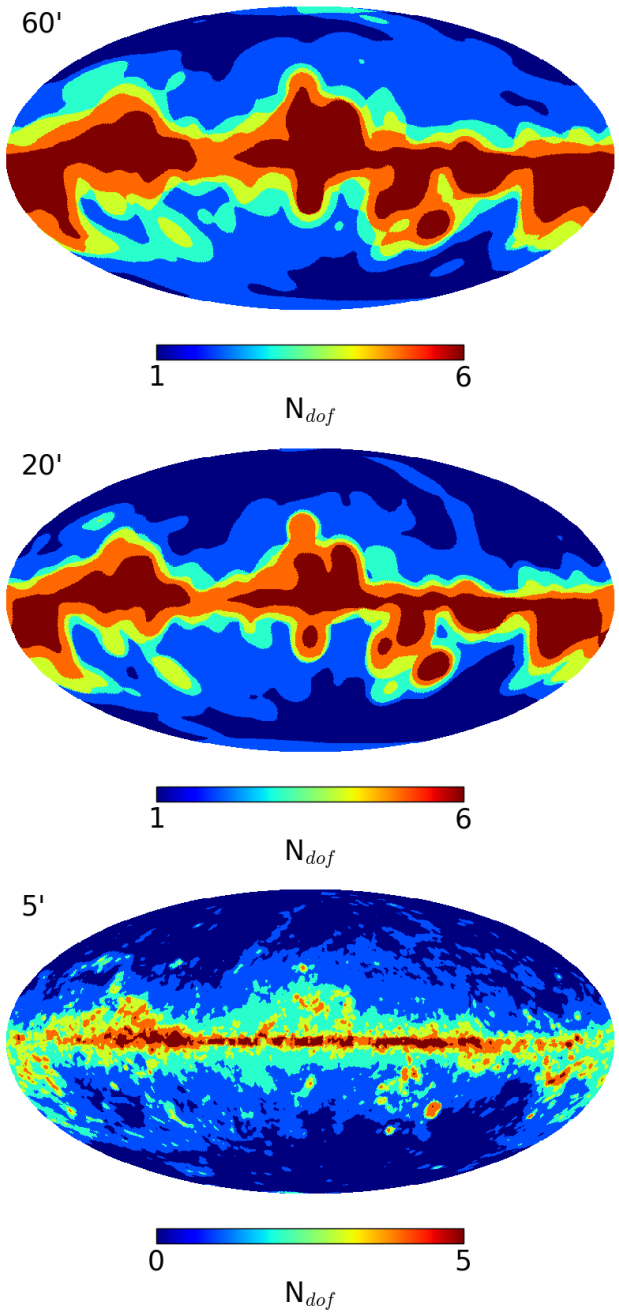

Fig. A.1. Local number of Galactic foreground degrees of freedom selected by the AIC criterion at one degree angular scale (*top*), 20′ scale (*middle*), and 5′ scale (*bottom*). The number of Galactic degrees of freedom decreases at high latitude and small angular scales.

A.4. Model selection with the Akaike information criterion

In Remazeilles et al. (2011b), the effective number, m, of Galactic components in each needlet domain was estimated by rejecting the eigenvalues in Eq. (A.22) that are smaller than 1.25, i.e. for which the "noise" contributes to the observation by more than 80%. This criterion is somewhat arbitrary. In the present work, we propose instead to use a statistical criterion to discriminate between the "large" eigenvalues, tracing the Galactic signal, and the "noisy" eigenvalues ($\approx$1) to be rejected; the effective rank of the covariance matrix of the Galactic signal is estimated by statistical model selection through the Akaike information criterion (Akaike 1974).

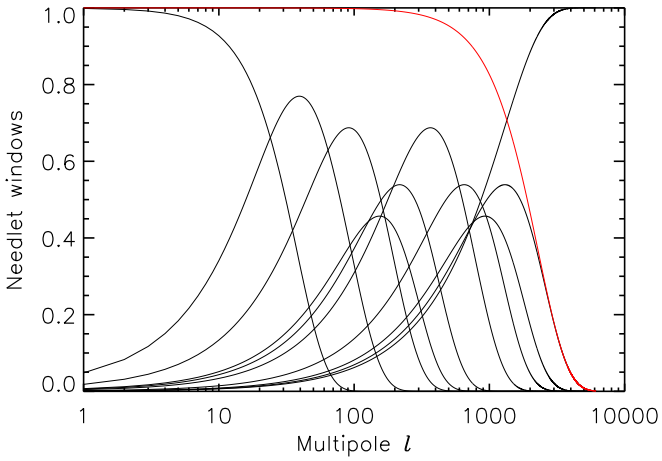

Fig. A.2. Needlet windows acting as bandpass filters in harmonic space (black lines), with the 5′ beam transfer function overplotted (red line).

For a given dimension, or model, m, if we assume that the data, $\boldsymbol{x}$, are independent and identically distributed according to the Gaussian distribution $\mathcal{N}(0, \mathsf{R}(m))$, with $\mathsf{R}(m) = \mathsf{R}_f(m) + \mathsf{R}_{\rm N}$, then the likelihood reads as

$$\mathcal{L}\left(\{\boldsymbol{x}_k\}_k|\mathsf{R}(m)\right) = \prod_{k=1}^{n} \frac{1}{\sqrt{2\pi \det \mathsf{R}(m)}} \exp\left\{-\frac{1}{2}\boldsymbol{x}_k^{\mathsf{T}}\mathsf{R}(m)^{-1}\boldsymbol{x}_k\right\}, \tag{A.33}$$

where n is the number of modes in the (needlet) domain considered. The log-likelihood can be written as

$$\begin{aligned} -2\log\mathcal{L} &= \sum_{k=1}^{n} \boldsymbol{x}_k^{\mathsf{T}}\mathsf{R}(m)^{-1}\boldsymbol{x}_k - \log\det\left(\mathsf{R}(m)^{-1}\right) + \text{constant}(m) \\ &= n\,K\left(\widehat{\mathsf{R}}, \mathsf{R}(m)\right) + \text{constant}(m), \end{aligned} \tag{A.34}$$

where $K\left(\widehat{\mathsf{R}}, \mathsf{R}(m)\right)$ is the Kullback-Leibler divergence (Kullback 1968), measuring the spectral mismatch between the model covariance matrix, $\mathsf{R}(m)$, and the data covariance matrix, $\widehat{\mathsf{R}}$:

$$K\left(\widehat{\mathsf{R}}, \mathsf{R}(m)\right) = \mathrm{Tr}\left(\widehat{\mathsf{R}}\mathsf{R}(m)^{-1}\right) - \log\det\left(\widehat{\mathsf{R}}\mathsf{R}(m)^{-1}\right) - N_{\rm ch}. \tag{A.35}$$

At this stage, it is interesting to note that the estimate of the Galactic covariance matrix, $\widehat{\mathsf{R}}_f(m)$ computed in Eq. (A.25), is nothing other than the maximum likelihood estimate, i.e. the minimizer of the Kullback-Leibler divergence of Eq. (A.35), as in SMICA (Delabrouille et al. 2003; Cardoso et al. 2008). The proof is given in Sect. A.5.

In the region of the sky and the range of angular scales considered, we select the best rank value, m^*, among the class of models, m, by minimizing the AIC

$$A(m) = 2\,n\,m - 2\log\left(\mathcal{L}_{\max}(m)\right). \tag{A.36}$$

Through the penalty, $2\,n\,m$, the AIC makes a trade-off between the goodness of fit and the complexity of the model. Let us denote $\widehat{\mathsf{R}}_{\rm N}^{-1/2}\widehat{\mathsf{R}}\widehat{\mathsf{R}}_{\rm N}^{-1/2} = \mathsf{U}\mathsf{D}\mathsf{U}^{\mathsf{T}}$ the diagonalization of the transformed data covariance matrix, where

$$\mathsf{U} = [\mathsf{U}_{\rm S}|\mathsf{U}_{\rm N}] \quad \text{and} \quad \mathsf{D} = \begin{bmatrix} \widehat{\mathsf{D}}_{\rm S} & 0 \\ 0 & \widehat{\mathsf{D}}_{\rm N} \end{bmatrix}. \tag{A.37}$$

Since the maximum likelihood is reached when $\widehat{\mathsf{R}}_{\rm N}^{-1/2}\widehat{\mathsf{R}}(m)\widehat{\mathsf{R}}_{\rm N}^{-1/2} = \mathsf{U}_{\rm S}\,(\mathsf{D}_{\rm S}-\mathsf{I})\,\mathsf{U}_{\rm S}^{\rm T}+\mathsf{I}$, we have

$$\begin{aligned}
-2\log\left(\mathcal{L}_{\max}(m)\right) &= nK\left(\widehat{\mathsf{R}}_{\rm N}^{-1/2}\widehat{\mathsf{R}}\widehat{\mathsf{R}}_{\rm N}^{-1/2}, \mathsf{U}_{\rm S}\,(\mathsf{D}_{\rm S}-\mathsf{I})\,\mathsf{U}_{\rm S}^{\rm T}+\mathsf{I}\right)\\
&= nK\left(\mathsf{D}, \mathsf{U}^{\rm T}\left[\mathsf{U}_{\rm S}\,(\mathsf{D}_{\rm S}-\mathsf{I})\,\mathsf{U}_{\rm S}^{\rm T}+\mathsf{I}\right]\mathsf{U}\right)\\
&= nK\left(\begin{bmatrix}\mathsf{D}_{\rm S} & 0\\ 0 & \mathsf{D}_{\rm N}\end{bmatrix}, \begin{bmatrix}\mathsf{D}_{\rm S} & 0\\ 0 & \mathsf{I}\end{bmatrix}\right)\\
&= n\left\{\mathrm{Tr}\left(\begin{bmatrix}\mathsf{I} & 0\\ 0 & \mathsf{D}_{\rm N}\end{bmatrix}\right) - \log\det\left(\begin{bmatrix}\mathsf{I} & 0\\ 0 & \mathsf{D}_{\rm N}\end{bmatrix}\right) - N_{\rm ch}\right\}\\
&= n\left(m + \sum_{i=m+1}^{N_{\rm ch}}\mu_i - \sum_{i=m+1}^{N_{\rm ch}}\log\mu_i - N_{\rm ch}\right)\\
&= n\left(m + \sum_{i=m+1}^{N_{\rm ch}} f(\mu_i)\right), \qquad \text{(A.38)}
\end{aligned}$$

where μ_i are the $(N_{\rm ch}-m)$ eigenvalues of the transformed data covariance matrix, $\mathsf{R}_{\rm N}^{-1/2}\widehat{\mathsf{R}}\mathsf{R}_{\rm N}^{-1/2}$, collected in the matrix $\mathsf{D}_{\rm N}$, and

$$f(\mu) = \mu - \log\mu - 1. \qquad \text{(A.39)}$$

This convex function is minimum for $\mu = 1$.

Therefore, the AIC criterion reduces to the simple analytical form:

$$A(m) = n\left(2\,m + \sum_{i=m+1}^{N_{\rm ch}}\left[\mu_i - \log\mu_i - 1\right]\right), \qquad \text{(A.40)}$$

and the dimension of the Galactic signal subspace is estimated by minimizing Eq. (A.40) in each region considered:

$$m^* = \mathrm{argmin}\,\left[A(m)\right]. \qquad \text{(A.41)}$$

Minimizing the AIC criterion (Eq. (A.40)) in each needlet domain (i.e. in each region of the sky and each range of angular scales) allows for estimating the effective dimension of the Galactic signal subspace locally, given the level of contamination by noise, CIB, and CMB in this region. The multi-dimensional ILC then adapts the filtering to the effective local dimension of the Galactic signal. In this respect, the GNILC method goes beyond the SMICA method by relaxing any prior assumption on the number of Galactic components.

Figure A.1 shows the local dimension of the Galactic signal subspace over the sky, for three different ranges of angular scales, which we have estimated by minimizing the AIC criterion (Eq. (A.40)) on the *Planck* data. In practice, the dimension of the Galactic signal subspace (equivalently, the number of Galactic degrees of freedom) clearly depends on the local signal-to-noise ratio, where the "noise" here includes the instrumental noise, the CIB, and the CMB signals. As expected, at high latitude and small angular scales (bottom panel in Fig. A.1) this number decreases because the CIB and the instrumental noise become dominant in the observations.

A.5. Minimization of the Kullback-Leibler divergence

To close this appendix, we show that the GNILC estimates of the covariance matrix (Eq. (A.25)) and the mixing matrix (Eq. (A.27)) are the maximum likelihood solution that minimizes the Kullback-Leibler divergence (Eq. (A.35)). For the sake of simplicity, we will assume that the data have been whitened so that the nuisance covariance matrix is represented by an identity matrix, I.

Let us consider a foreground model with a fixed number, m, of independent templates in the domain being considered. The foreground covariance matrix can therefore be modelled as a rank–m matrix

$$\mathsf{R}_f(m) = \mathsf{A}_m\Lambda_m\mathsf{A}_m^{\rm T}, \qquad \text{(A.42)}$$

and the full data covariance matrix as

$$\mathsf{R}(m) = \mathsf{A}_m\Lambda_m\mathsf{A}_m^{\rm T} + \mathsf{I}, \qquad \text{(A.43)}$$

where Λ_m is an $m\times m$ diagonal matrix collecting the m non-null eigenvalues of $\mathsf{R}_f(m)$ and A_m is an $N_{\rm ch}\times m$ matrix collecting the m corresponding eigenvectors. In other words, the eigendecomposition of the foreground covariance matrix is given by

$$\mathsf{R}_f(m) = [\mathsf{A}_m\mathsf{A}_{N_{\rm ch}-m}]\begin{bmatrix}\Lambda_m 0\\ 0\;0\end{bmatrix}[\mathsf{A}_m\mathsf{A}_{N_{\rm ch}-m}]^{\rm T}. \qquad \text{(A.44)}$$

The maximum likelihood estimate, Λ_m, minimizing the Kullback-Leibler divergence, must satisfy for all $(i,j)\in[1,m]^2$

$$\begin{aligned}
\frac{\partial K\left(\widehat{\mathsf{R}}, \mathsf{R}(m)\right)}{\partial(\Lambda_m)_{ij}} &= \\
&-\mathrm{Tr}\left(\widehat{\mathsf{R}}\mathsf{R}(m)^{-1}\frac{\partial\mathsf{R}(m)}{\partial(\Lambda_m)_{ij}}\mathsf{R}(m)^{-1}\right) + \mathrm{Tr}\left(\mathsf{R}(m)^{-1}\frac{\partial\mathsf{R}(m)}{\partial(\Lambda_m)_{ij}}\right)\\
&= -\frac{\left(\mathsf{A}_m^{\rm T}\widehat{\mathsf{R}}\mathsf{A}_m\right)_{ij}}{((\Lambda_m)_{ii}+1)\left((\Lambda_m)_{jj}+1\right)} + \frac{\delta_{ij}}{((\Lambda_m)_{ii}+1)}\\
&= 0. \qquad \text{(A.45)}
\end{aligned}$$

Therefore, the maximum likelihood estimate, $\{\mathsf{A}_m, \Lambda_m\}$, is solution of

$$\left(\mathsf{A}_m^{\rm T}\widehat{\mathsf{R}}\mathsf{A}_m\right) = (\Lambda_m + \mathsf{I}). \qquad \text{(A.46)}$$

where I is an $m\times m$ identity matrix. If we consider the eigenvalue decomposition of the full data covariance matrix as

$$\widehat{\mathsf{R}} = \mathsf{U}\mathsf{D}\mathsf{U}^{\rm T} = [\mathsf{U}_{\rm S}\mathsf{U}_{\rm N}]\begin{bmatrix}\mathsf{D}_{\rm S} & 0\\ 0 & \mathsf{D}_{\rm N}\end{bmatrix}[\mathsf{U}_{\rm S}\mathsf{U}_{\rm N}]^{\rm T} \qquad \text{(A.47)}$$

where $\mathsf{D}_{\rm S}$ is the $m\times m$ diagonal matrix collecting the m largest eigenvalues of $\widehat{\mathsf{R}}$, and $\mathsf{U}_{\rm S}$ is an $N_{\rm ch}\times m$ matrix collecting the m corresponding eigenvectors, then the maximum likelihood solution of Eq. (A.46) is given by

$$\begin{aligned}
\Lambda_m &= \mathsf{D}_{\rm S} - \mathsf{I},\\
\mathsf{A}_m &= \mathsf{U}_{\rm S}. \qquad \text{(A.48)}
\end{aligned}$$

A.6. Test on Planck simulations

We apply the GNILC algorithm to the public[5] *Planck* full focal plane simulations (FFP8) from Planck Collaboration XII (2016) in order to validate the component-separation method.

We still adopt as a prior for GNILC the *Planck* 2013 CIB best-fit power spectra, although the simulations of the CIB components in FFP8 do not follow the exact same statistics, since the FFP8 CIB maps are generated across frequencies from simulated dark matter shells in Planck Collaboration XII (2016). The imperfect agreement between the prior and the actual CIB power spectrum enables us to test the robustness of GNILC when the knowledge of the CIB power spectrum is not perfect.

In Fig. A.3 we compare the reconstructed GNILC dust map with the input FFP8 dust map within some small CIB fields of Planck Collaboration XXX (2014), where the dust is faint,

[5] http://crd.lbl.gov/cmb-data

namely NEP4 (part of the GHIGLS NEP field) and SP. The difference between the GNILC dust map and the input dust map is also shown. In Fig. A.4, we compare the reconstructed GNILC CIB map with the input FFP8 CIB map. The difference between the GNILC CIB and the input CIB is shown in the third column of Fig. A.4.

The T–T correlation between the GNILC output dust and the FFP8 input dust is plotted in Fig. A.5. The T–T correlation between the GNILC output CIB and the FFP8 input CIB is plotted in Fig. A.6. In the NEP4 field, the slope of the T–T scatter plots is 0.997 ± 0.006 for the dust and 0.981 ± 0.008 for the CIB. In the SP field, the slope of the T–T scatter plots is 0.997 ± 0.006 for the dust and 1.079 ± 0.008 for the CIB. In both fields, the Pearson correlation coefficient between the input and the GNILC reconstruction is found larger than 0.9 for the dust and larger than 0.8 for the CIB.

The successful reconstruction of dust and CIB shows that the GNILC method is robust to imperfect prior assumptions on the CIB angular power spectra. As shown in Olivari et al. (2016), it is not the exact morphology of the CIB power spectrum but the overall slope that matters for enabling GNILC to discriminate between dust and CIB. The prior power spectrum in GNILC is only intended to estimate the dimension of the dust and CIB component subspaces (Sect. A.3) not the amplitude of these components (Sect. A.1).

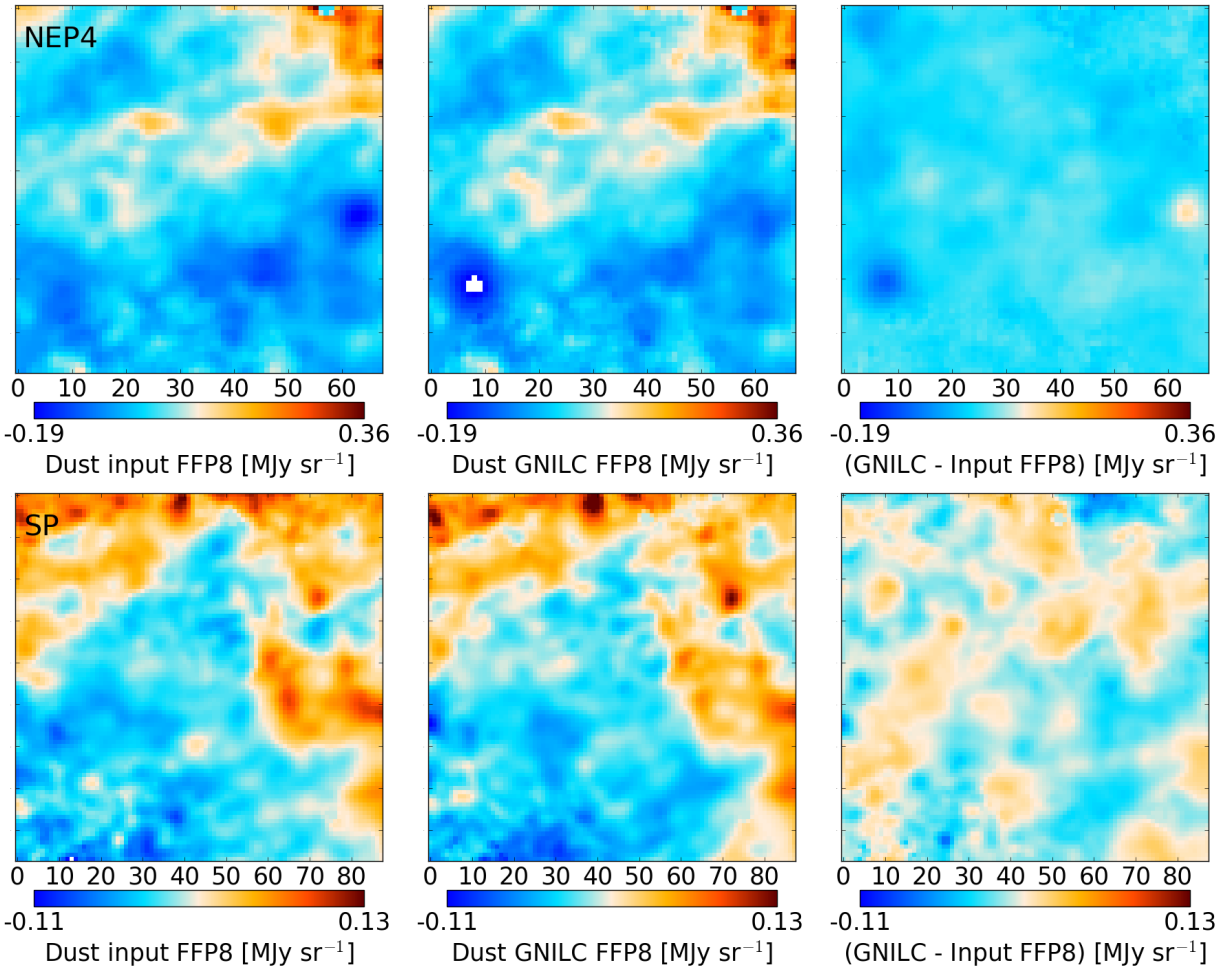

Fig. A.3. Thermal dust maps from the *Planck* FFP8 simulations. Input dust FFP8 (*left*), GNILC dust FFP8 (*middle*), difference (GNILC – input) (*right*). The fields are: NEP4 (*top*) and SP (*bottom*).

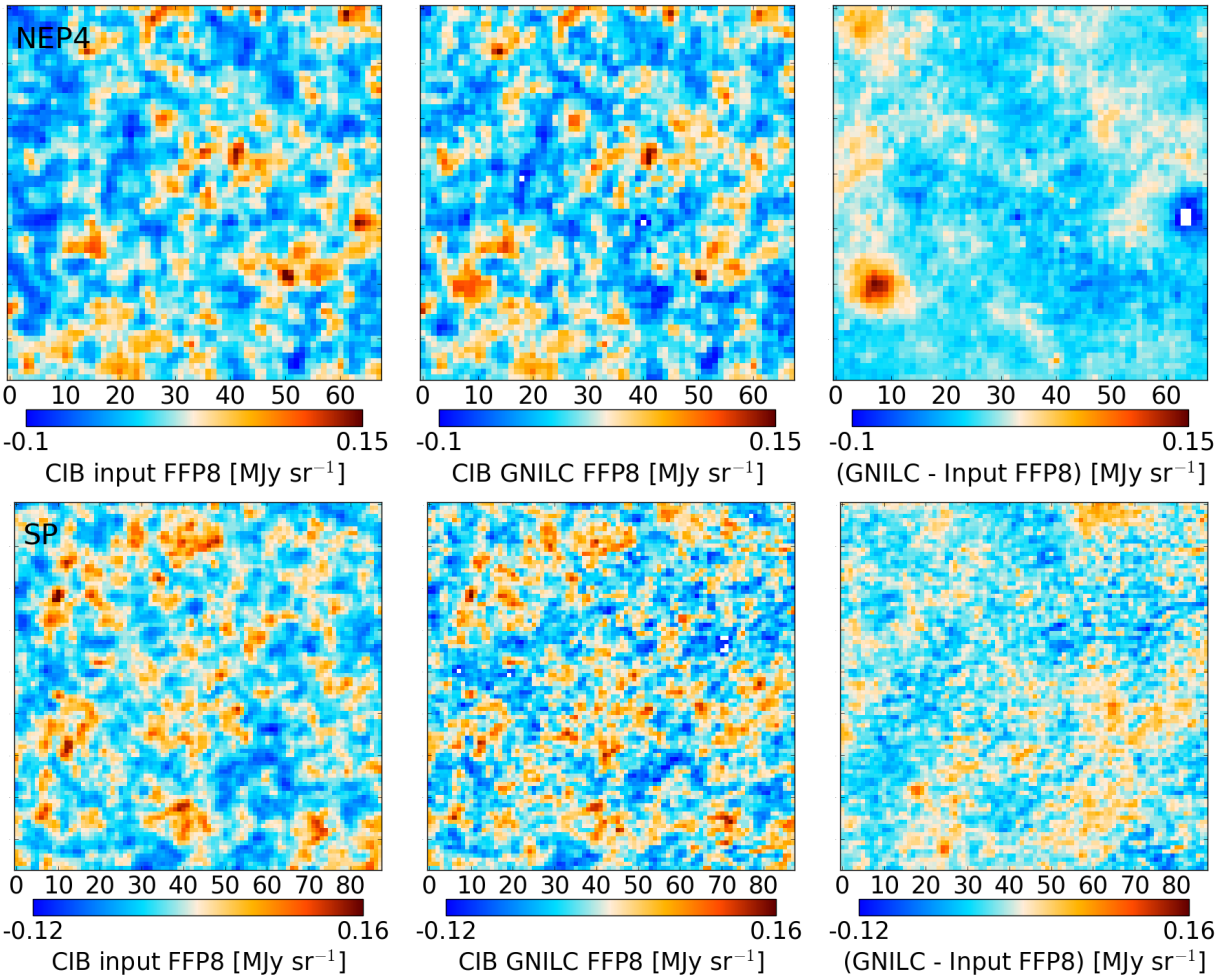

Fig. A.4. CIB maps from the FFP8 simulations. Input CIB FFP8 (*left*), GNILC CIB FFP8 (*middle*), difference (GNILC – input) (*right*). The fields are: NEP4 (*top*) and SP (*bottom*).

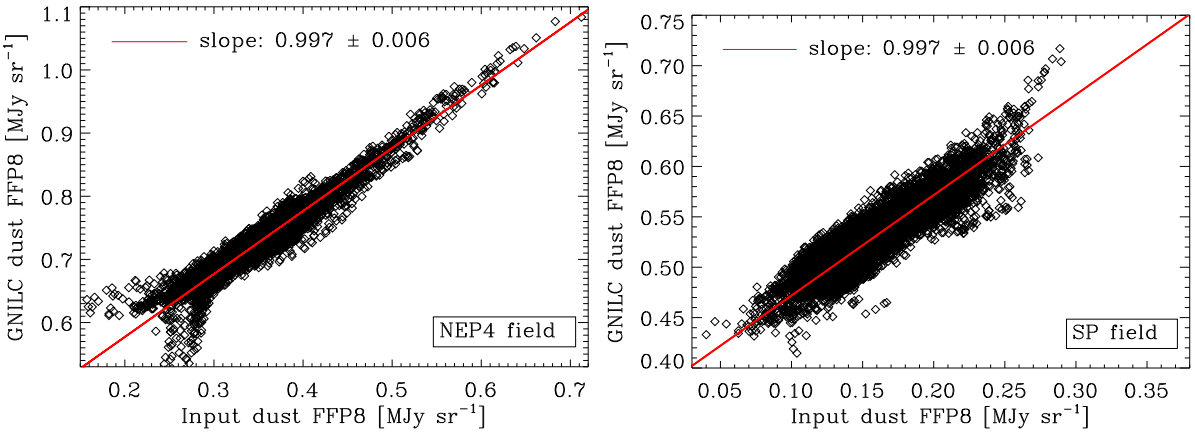

Fig. A.5. *T*–*T* scatter plots of the *Planck* FFP8 simulations between GNILC and the input thermal dust maps in the NEP4 field (*left*) and the SP field (*right*).

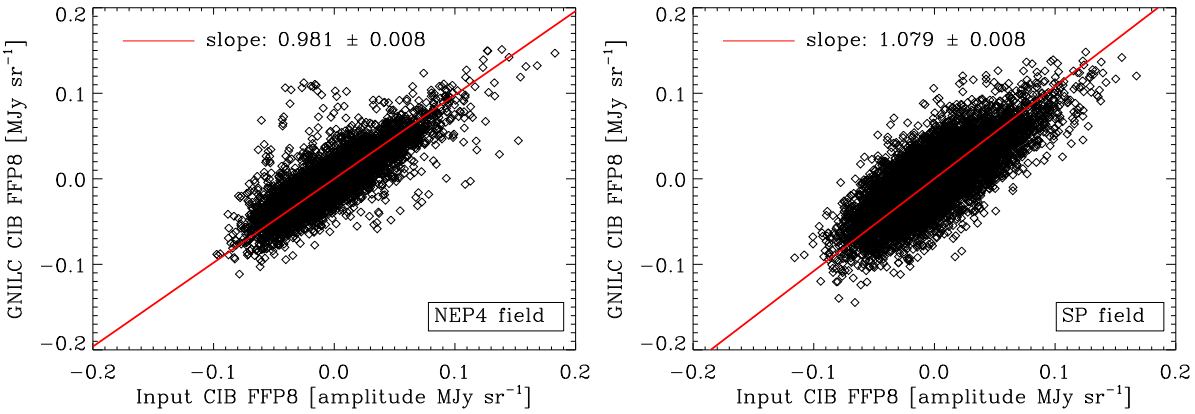

Fig. A.6. *T*–*T* scatter plots of the *Planck* FFP8 simulations between GNILC and input CIB maps in the NEP4 field (*left*) and the SP field (*right*).